Chapter 8

EPR in glass ceramics

Andris Antuzevics*

Institute of Solid State Physics, University of Latvia, Riga, Latvia

**Corresponding author: Email address: andris.antuzevics@cfi.lu.lv (A. Antuzevics)*

Chapter Outline Head

8.1. INTRODUCTION

Glass ceramics are composite materials, which contain one or more crystalline phases within an amorphous glassy phase. If crystallites are small enough (smaller than the wavelength of visible light, usually around 20–50 nm), transparency of the glass ceramic material can be maintained. The idea of developing transparent and durable materials with single crystal like optical performance at a reduced cost has attracted a considerable scientific effort. These materials could be used as white light sources [1–8], infrared radiation up-converters [9–16], or temperature sensors [17–19]. Incorporation of activators in

the crystalline phase is necessary in order to achieve the desired optical properties of glass ceramics. Luminescence characteristics are also influenced by atomic arrangements within the crystallites themselves; therefore, local environment sensitive analysis methods must be applied. Magnetic resonance spectroscopy techniques can provide valuable insights about local atomic surroundings of paramagnetic ions. This chapter will overview the results of recent continuous wave EPR spectroscopy studies of glass ceramic systems. First, some general concepts and methods for characterizing these materials will be introduced. For a more detailed description of these aspects, the reader is advised to turn to review articles and books devoted to glass ceramics (e.g., Refs. [20–26]).

## 8.2. PREPARATION AND CHARACTERIZATION OF GLASS CERAMICS

One of the simplest approaches in glass ceramics' synthesis is thermal treatment of a precursor glass obtained by the melt-quenching technique. In this two-step process: first, a chosen composition of powder ingredients is melted and rapidly quenched afterward, usually by pouring the melt onto a stainless steel, brass or graphite mold. The melt-quenching process is pictured in Fig. 1.

A subsequent thermal treatment below the melting temperature is often necessary to precipitate crystallites in the glass matrix. When annealed, the precursor glass may form ordered crystalline structures within the matrix. In order to maintain the transparency of the final product, a homogeneous crystallization and uniform distribution of nanoparticles is required. The structure of a glass and glass ceramic is schematically illustrated in Fig. 2.

Electron microscopy techniques can be employed for a direct visualization of the precipitated nanostructures. Typical scanning electron microscopy

FIG. 1   The melt quenching process of a glass. *Photography by Dr. Andris Fedotovs.*
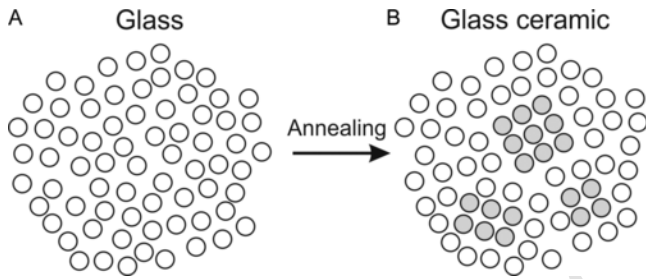
FIG. 2   Schematic (A) glass and (B) glass ceramic structure illustrations.

(SEM) images of glass and glass ceramic samples are shown in Fig. 3. The darker areas are formed by the lighter element ions of the glass matrix, whereas the white droplets indicate presence of crystallites containing heavier ions. Such micrographs allow the determination of particle size and distribution in the matrix.

SEM analysis is applicable for glass ceramics with relatively large nanocrystals, preferably with considerable deviations in the chemical composition of the crystalline and amorphous phases. For most other cases, transmission electron microscopy (TEM) is more suitable; where, similar to SEM, information about the structure and morphology of glass ceramics can be obtained. Typical TEM images are shown in Fig. 4. Particularly in the high resolution mode (HRTEM), one can even see the ordered structure of nanocrystals and measure the distances between the atomic planes.

As the process of crystallization usually requires additional annealing of the precursor glass, it is crucial to investigate samples' responses to thermal treatment. Differential thermal analysis (DTA) and differential scanning calorimetry techniques allow the determination of the glass transition temperature T_g and temperatures corresponding to different crystallization processes. During a DTA measurement, the heat flow in comparison to a reference sample is continuously monitored to detect temperatures at which thermodynamic
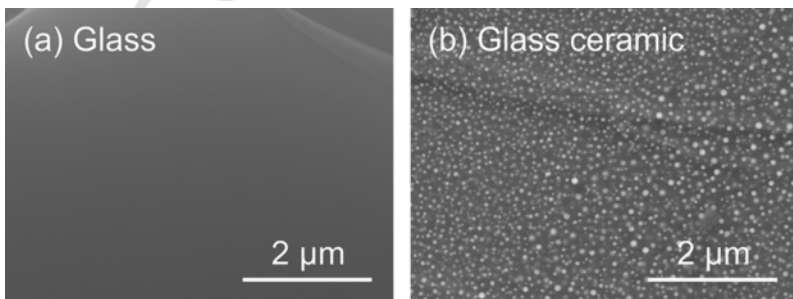

FIG. 3   SEM images of an oxyfluoride (A) glass and (B) glass ceramic. *Micrographs by Guna Krieke.*
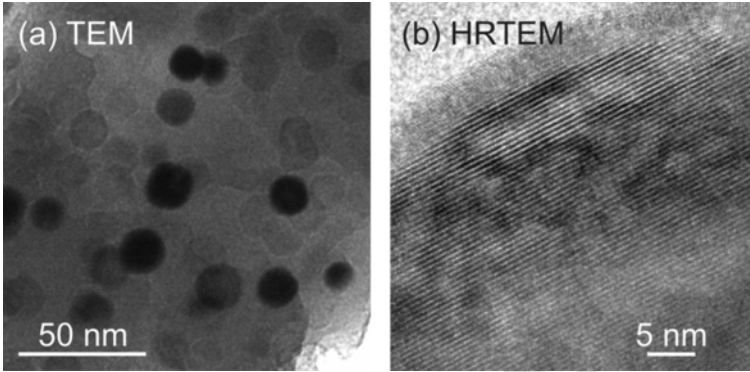
FIG. 4   (A) TEM and (B) HRTEM images of an oxyfluoride glass ceramic containing SrF_2 nanocrystals. *Micrographs by Dr. Krisjanis Smits.*

changes of state occur. An example of a DTA curve is shown in Fig. 5. T_g marks the temperature range where the rigid glass structure transforms into a more viscous state. Here the exothermic peaks at T_{C1} and T_{C2} corresponds to the crystallization of the primary phase SrF_2 and the bulk crystallization of the glass matrix itself. Annealing the sample at a temperature between T_{C1} and T_{C2} is expected to precipitate SrF_2 as the only crystalline phase.
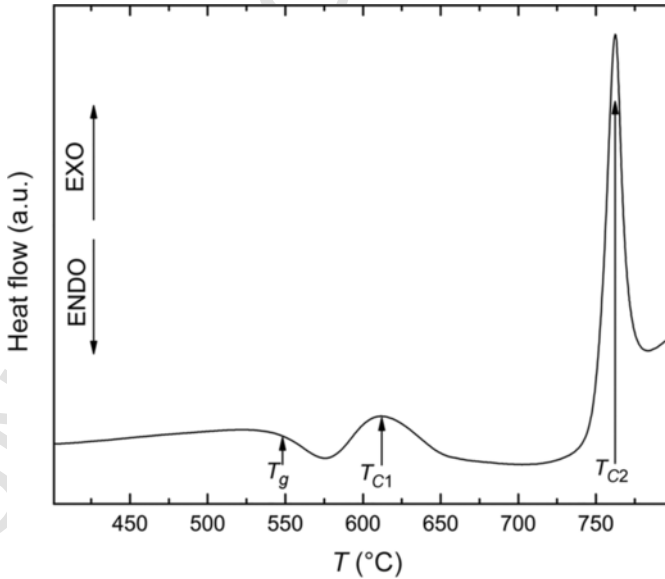

FIG. 5   DTA curve of a glass sample (nominal composition: 40-SiO_2–25Al_2O_3–15Na_2CO_3–19SrF_2–1EuF_3).

X-ray diffraction measurements (XRD) are commonly used to identify crystalline phases present in glass ceramics. The sharp peaks in diffraction patterns corresponding to specific interplanar distances in the crystalline lattice are the "fingerprints" of the specific nanocrystals present in the samples. Typical XRD patterns are shown in Fig. 6. The precursor glass has a broad background signal indicating a lack of long-range order as could be expected from a disordered system. After a 1 h long heat treatment at a temperature between T_{C1} and T_{C2} formation of SrF_2 nanocrystals occurs. Annealing above T_{C2} produces a ceramic sample that consists of various silicate phases. The average crystallite size D can be estimated from the XRD data using the Scherrer equation [27]:

$$D = \frac{K\lambda}{\beta \cos \theta} \tag{1}$$

where K is a numerical factor, λ is the wavelength of X-rays used in the experiment, β is the full width at half maximum of the XRD peak, and θ is the scattering Bragg angle. For example, the average size of SrF_2 nanocrystals in Fig. 6 estimated from Eq. (1) is ≈ 20 nm. It should be noted that the Scherrer equation is only applicable for crystals smaller than ≈ 100 nm. In some cases, other factors, such as uneven distribution of activators, can contribute to the broadening of XRD peaks.
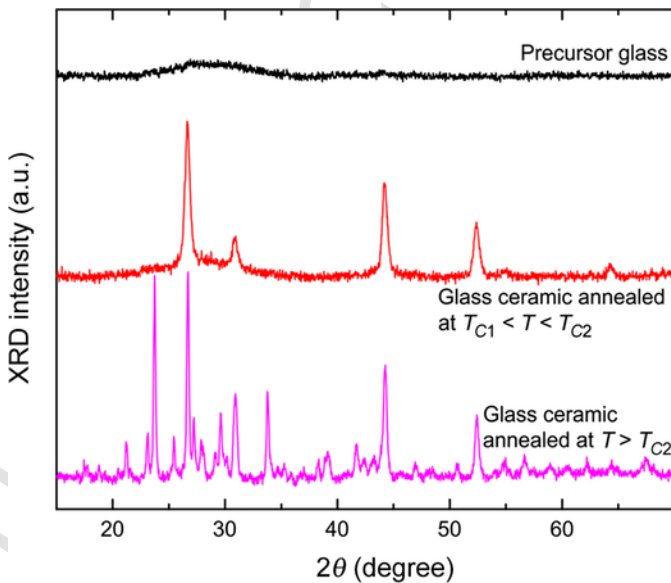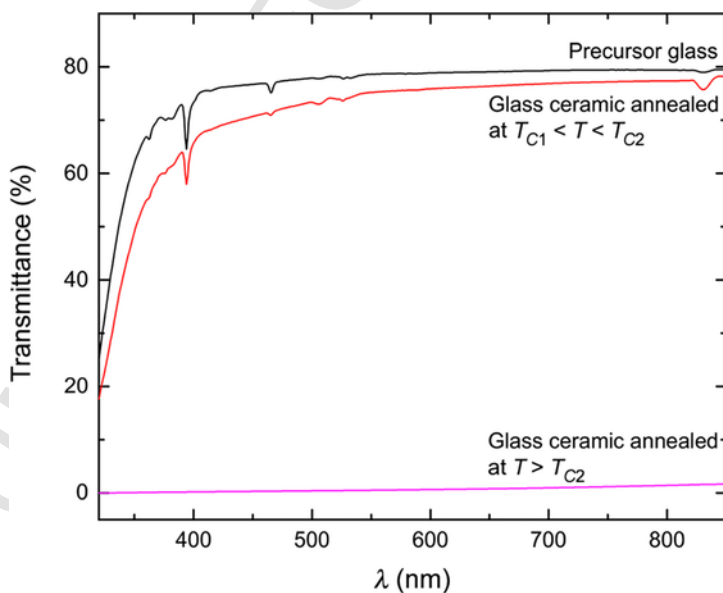

FIG. 6   XRD patterns of a precursor glass and glass ceramic samples obtained after thermal treatment (nominal composition: $40SiO_2–25Al_2O_3–15Na_2CO_3–19SrF_2–1EuF_3$).

Controlling the size of nanoparticles is essential for maintaining the transparency of glass ceramics. For a system with a refractive index difference between the glass and crystalline phases of 0.3, the diameter of crystallites should not exceed 40 nm [21]. Larger crystallites will significantly scatter incident light, leading to an opaque appearance of the sample. The transparency spectra of glass or glass ceramic containing single phase SrF_2 nanocrystals (annealed between T_{C1} and T_{C2} for 1 h) and ceramic (annealed above T_{C2} for 1 h) samples are shown in Fig. 7.

Spectroscopic techniques enable further characterization of glass ceramics. Complementary Raman and infrared spectra contain information about the nature of bonds in the samples. The short range order can additionally be analyzed using solid-state nuclear magnetic resonance and X-ray absorption spectroscopy. The luminescence behavior of dopant ions is local structure sensitive and usually requires the use of conventional as well as time-resolved and site-selective spectroscopy techniques to be fully understood. A photograph of luminescent transparent oxyfluoride glass ceramics doped with Eu^{3+}, Tb^{3+} and Eu^{2+} is shown in Fig. 8.

The power of EPR spectroscopy lies in the ability to probe the electronic structure of paramagnetic defects very precisely. Resonance positions in EPR spectra are sensitive to various interactions; the paramagnetic center is involved in conveying valuable information about its local environment. In many cases, an unambiguous defect model assignment is possible, which is

FIG. 7   Transmittance spectra of a precursor glass and glass ceramic samples obtained after thermal treatment (nominal composition: $40SiO_2$–$25Al_2O_3$–$15Na_2CO_3$–$19SrF_2$–$1EuF_3$).

FIG. 8 Luminescence of rare earth ion doped (*red* (*dark gray* in the print version)—Eu^{3+}; *green* (*light gray* in the print version)—Tb^{3+}; *blue* (*gray* in the print version)—Eu^{2+}) transparent glass ceramics under UV excitation. *Photography by Dr. Andris Fedotovs.*

particularly helpful in investigations of complex composite glass ceramic materials.

8.3. EPR INVESTIGATIONS OF GLASS CERAMICS

8.3.1 General aspects of EPR spectroscopy

The main principle of EPR is similar to other fields of spectroscopy—changes in incident electromagnetic radiation as it passes through the sample contain information about energy levels of the absorbing species. By means of EPR spectroscopy paramagnetic centers—point defects with unpaired electrons—can be studied. As the name of the method suggests, external magnetic field B is necessary to split the spin states and microwave frequency; electromagnetic radiation can be applied to excite transitions between these states. Thus a typical EPR spectrum displays the first derivative of microwave absorption vs B.

The resonance positions in EPR spectra depend on the local atomic arrangements and various interactions the paramagnetic center is involved in. This can be expressed through the spin-Hamiltonian (SH) formalism [28,29]:

$$H = \mu_B B \cdot g \cdot S + \sum_{k,q} B_k^q O_k^q + S \cdot A \cdot I \tag{2}$$

where the first term is the Zeeman interaction, the second—zero field splitting (ZFS) and the third—the hyperfine (HF) interaction. In Eq. (2) μ_B is the Bohr magneton; S—the effective spin of the paramagnetic center; I—the spin of in-

teracting nucleus; g, A—Zeeman and HF interaction tensors respectively; B_k^q—ZFS interaction parameters and O_k^q—the extended Stevens operators. Higher order terms are usually not resolved in continuous wave X-band EPR experiments and are not included in Eq. (2).

One can immediately notice the technical hardship to be overcome for a successful interpretation of EPR spectra. The situation is further aggravated by the abundance of different notations of SH terms and their parameters used by EPR practitioners [28]. Therefore, unfortunately, EPR spectroscopy is often inaccessible by non-specialists in the field. For a thorough general introduction to EPR, the reader is advised to consult Refs. [29–33].

Eq. (2) allows for the calculation of energy levels of a spin system as a function of B. In EPR experiments, microwave quanta with energy $h\nu$ are applied to excite the resonant transitions. A successful fitting of the experimental spectrum enables the extraction of the SH parameters (g, B_k^q and A). The parameters in turn reflect information about the local environment around the defect site. First, only systems with $S \neq 0$ will produce any EPR signal at all. For systems with $S > 0$, the Zeeman interaction term describes the linear energy dependence of spin sublevels M_S on the external magnetic field value. This term is quantified by the g value, which is often referred to as the "fingerprint" of the spin system. EPR interactions are generally angle-dependent on the paramagnetic center orientation in respect to B; therefore, the interaction parameters are, in fact, matrices. In case $S > 1/2$, the ZFS term also should be included in the SH. As the name suggests, its effects are present already in the absence of B. The non-zero parameters B_k^q depend on the S value as well as the local site symmetry. If magnetic nuclei ($I \neq 0$) are nearby, the HF structure may be resolved in the spectrum. S interaction with one nuclear spin I will cause additional splitting of the resonances into $2I + 1$ components. The magnitude of splitting is determined by the value of A. Interaction with nuclei other than the one the electron shell is bound to is also possible and in EPR spectroscopy is historically referred to as the superhyperfine (SHF) interaction.

Another important aspect in addition to the spin system is the host matrix under study. In single crystal samples, angle-dependent resonance spectra can be recorded. Polycrystalline samples consist of randomly oriented micro/nano-sized single crystals; therefore, one can expect the average EPR spectrum of all the possible single crystal orientations. Averaging across a myriad of different orientations leads to significantly broader spectral features in comparison to single crystal spectra. In disordered media, such as glasses, each paramagnetic center is additionally located in a slightly different local environment. In general, this is taken into account by statistical distributions of the relevant SH parameters. It is convenient to define effective g values to refer to the most prominent features of glass EPR spectra [34]:

$$g_{eff}\mu_B B_{res} = h\nu \tag{3}$$

g_{eff} values are not necessarily related to the g tensor in Eq. (2).

What peculiarities could we expect in the EPR spectra of glass ceramics? If amorphous, EPR spectra of the initially casted samples should have the same characteristics as typical glasses [34]. The heat treatment procedure produces chaotically oriented nanocrystals within the glass matrix; therefore, similar paramagnetic centers (i.e., separate powders) could form. Depending on the crystallite size, a contribution from paramagnetic centers located at the interface between the amorphous and crystalline media might also be detectable. As a result, a superposition of several signals is expected in a characteristic EPR spectrum of glass ceramics.

As many industrial applications of glass ceramics revolve around the luminescence of activator ions, it is both of fundamental and practical interest to characterize the incorporation, local structure, and properties of different paramagnetic point defects in these systems. On the other hand, the glass ceramic system may also be used as an educational tool to illustrate the formation of ordered structures within an amorphous phase. As will be shown, this allows the demonstration of various physical aspects of EPR spectroscopy and solid state physics in general.

The experimental EPR spectra in this chapter have been measured with a custom-built X-band ($\nu \approx 9.2$ GHz) EPR spectrometer at room temperature. Spectra simulations have been performed with EasySpin simulation toolbox [35].

8.3.2 Mn^{2+}

Mn^{2+} is a $3d^5$ configuration $S = 5/2$ ion with the resulting ground state $^6S_{5/2}$; therefore, the deviation from the $g_e = 2.0023$ is minimal. The 100% abundant ^{55}Mn isotope has a nuclear spin of $I = 5/2$, which produces a $2I + 1 = 6$ HF component pattern in the EPR spectrum. As a consequence, all terms of Eq. (2) are relevant for Mn^{2+} spectra analysis.

X-band EPR spectra of Mn^{2+} in glasses are remarkably similar to each other—the signature sextet due to the HF interaction with $I = 5/2$ at around $g_{eff} = 2.0$ is usually superimposed by a much broader signal [34,36–38]. Computer simulations reveal that g and A are less sensitive to variations in Mn^{2+} local environment in glasses; whereas a rather broad distribution in second order ZFS parameter B_2^0 and B_2^2 values is expected [39–41].

Several effects observed in manganese-doped glass ceramics are illustrated in EPR spectra shown in Figs. 9 and 10.

First, an intensity increase of the hyperfine sextet centered at $g_{eff} \approx 2$ relative to the shoulder spanning from 0.18 to 0.28 T is observed similarly as in Ref. [43]. Thus, upon the crystallization process, more Mn^{2+} ions are located
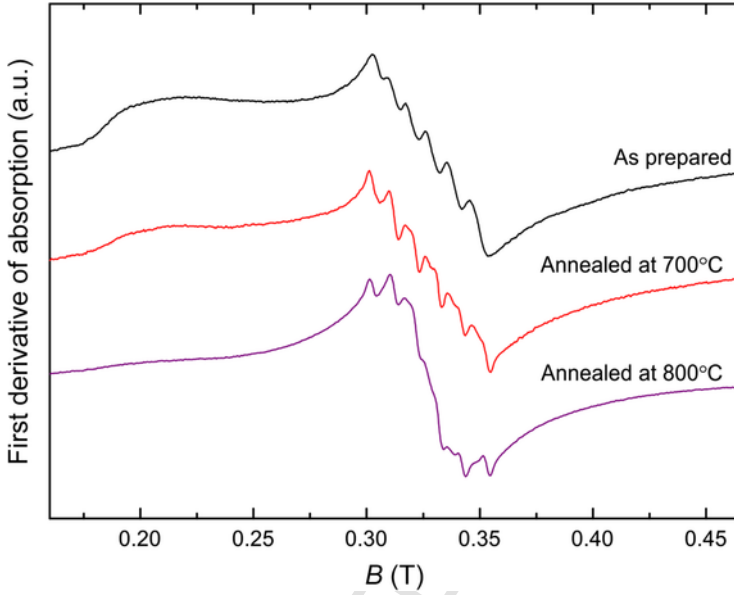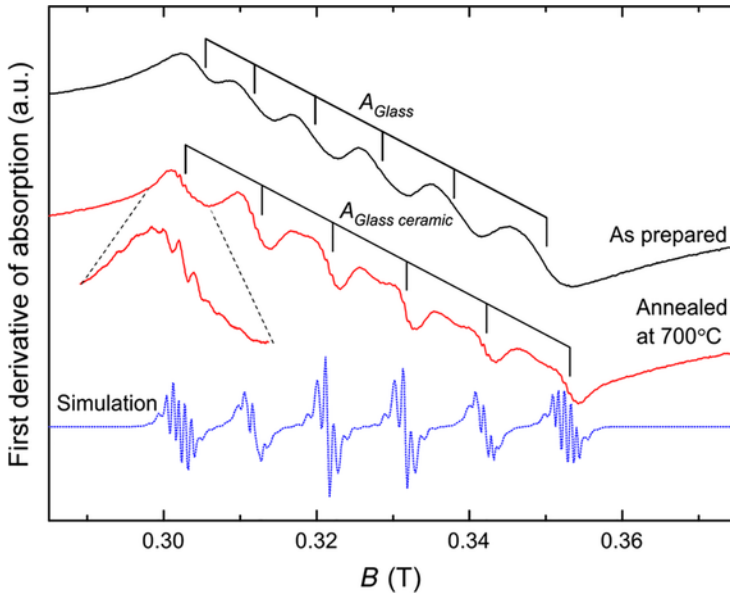
FIG. 9   EPR spectra of manganese doped precursor glass and glass ceramic samples (nominal composition: $40SiO_2–25Al_2O_3–15Na_2CO_3–20SrF_2–0.1MnF_2$).

in sites with high crystal field symmetry. Similar EPR spectra shapes have been observed in manganese doped lithium disilicate [44] and tellurite borate [45] glass ceramics. Second, the heat-treated samples exhibit narrower lines, indicating a smaller distribution of SH parameter values.

    A closer inspection shown in Fig. 10 reveals that the separation of the HF structure lines determined by the A value is different in the glass and glass ceramic samples. Here $A_{Glass} \approx 260$ MHz; $A_{Glass\ ceramic} \approx 280$ MHz. The value of A is dependent on the host matrix of the paramagnetic ion, and it correlates with the electronegativity of the surrounding ligands [46]. Thus Mn^{2+} ions in the glass ceramic sample have a more ionic bonding with the surrounding ions. Additionally, a sub-structure absent in the glass sample emerges after the annealing. In the case of Mn^{2+} centers in fluorides, an interaction with F^- ions with $I = 1/2$ is often resolved [42]. The spectrum in Fig. 10 is simulated with the cubic $SrF_2{:}Mn^{2+}$ center parameters. The splitting of each Mn^{2+} HF line numerous SHF components is caused by eight equidistant F^- ions in the first coordination sphere of the center. The SH (2) in simulations must be modified accordingly:

$$H = \mu_B B \cdot g \cdot S + S \cdot A_{Mn} \cdot I_{Mn} + \sum_i S \cdot A_{Fi} \cdot I_{Fi} \tag{4}$$

FIG. 10 EPR spectra of manganese doped precursor glass and glass ceramic samples (nominal composition: $40SiO_2$–$25Al_2O_3$–$15Na_2CO_3$–$20SrF_2$–$0.1MnF_2$). *Inset* shows a spread-out section of the region indicated by the *dashed lines*. Simulation with cubic SrF_2:Mn^{2+} center parameters from Ref. [42].

Observation of the SHF structure suggests that Mn^{2+} ions incorporate a high symmetry environment of the material. Similar SHF patterns have been observed when Mn^{2+} ions incorporate CaF_2 [47,48], SrF_2 [49] and BaF_2 [50] crystalline phases of oxyfluoride glass ceramics.

8.3.3 Cu^{2+}

$3d^9$ Cu^{2+} ion EPR spectra are easily distinguishable on the basis of their relatively large axial g anisotropy. Another distinctive feature is the four-component HF structure due to a combined 100% abundance of ^{63}Cu and ^{65}Cu nuclei ($I = 3/2$). As $S = 1/2$, the ZFS term is absent in Cu^{2+} EPR spectra [34,36]. For the case of axial symmetry and absence of ZFS, it is common to rewrite SH (2) in the following form:

$$H = \mu_B g_\parallel B_z S_z + \mu_B g_\perp \left(B_x S_x + B_y S_y\right) + A_\parallel S_z I_z + A_\perp \left(S_x I_x + S_y I_y\right) \qquad (5)$$

In glasses, it has been observed that the g tensor component values $g_\parallel > g_\perp > 2$ indicating that Cu^{2+} ions occupy sixfold coordinated sites of distorted octahedral symmetry [37,51–53]. Changes in Cu^{2+} SH parameter values, depending on the composition, allow the study of crystal field variations as well as the nature of bonds with the surrounding ligands.

Although Cu^{2+} ions in glasses have been investigated extensively, EPR studies of copper-doped glass ceramics are scarce. In fluoroindate glass ceramics, variations in EPR spectra shapes have been observed with g values in the crystallized samples corresponding well with the ones reported for crystalline Ba_2ZnF_6 [43]. However, the HF structure was not clearly resolved. A Gaussian-shape resonance line at $g_{eff} = 1.992$ also emerged, which was attributed to water content in the atmosphere during the preparation of glass ceramics [43]. A similar feature has been observed in oxyfluoride glass ceramics containing CaF_2 nanocrystals [47].

Let's take a closer look at the EPR spectra of a copper-doped oxyfluoride glass and glass ceramics in Fig. 11. The broad tail in the lower magnetic field region is characterized by the HF splitting of the $g_{||}$ component, whereas the features at ≈ 0.32 T are reflected in $g_\perp$ and $A_\perp$ values. The simulation curve represents Cu^{2+} center observed in single crystal CaF_2 [42]. The simulated resonances are absent in the glass ceramic sample containing CaF_2 nanocrystals; thus, it can be concluded that sixfold coordinated Cu^{2+} sites in the glass matrix are energetically more favorable than the eightfold coordinated sites in the crystalline phase.

In continuous wave X-band EPR studies of fluorosilicate glass ceramic systems, significant changes in the Cu^{2+} ion spectra shape after the thermal treatment procedure also have not been detected [54].
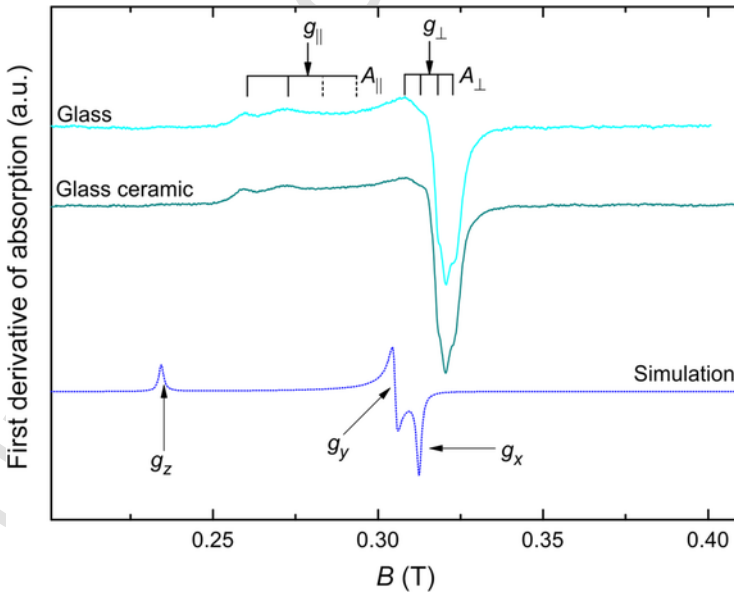

FIG. 11   EPR spectra of copper doped precursor glass and glass ceramic samples (nominal composition: $46SiO_2$–$20Al_2O_3$–$8CaCO_3$–$26CaF_2$–$0.1CuO$). Simulation with $CaF_2:Cu^{2+}$ center SH parameters from Ref. [42].

8.3.4 Cr^{3+}

The valence states of chromium can range from $+1$ to $+6$; however, the $3d^3$ Cr^{3+} state is the most stable one. EPR spectra of $S = 3/2$ Cr^{3+} ions are strongly influenced by the local site symmetry determined by ZFS parameters B_2^0 and B_2^2. In glasses, a large separation between the $M_S = \pm 3/2$ and $M_S = \pm 1/2$ Kramers doublets leads to resonances in the $g_{eff} \approx 2$–5 region [55–61]. Exchange coupled Cr^{3+} pairs have been attributed to a resonance near $g_{eff} \approx 2$ [55,58,59,61]; however, weakly distorted Cr^{3+} also may have spectral features in the same region [58–60].

EPR spectrum of a chromium-doped oxyfluoride glass is shown in Fig. 12. The resonances observed at $g_{eff} = 5.10$ and $g_{eff} = 1.97$ are in a good agreement with Cr^{3+}-doped glass system studies previously mentioned. The resonance at $g_{eff} = 4.3$ could be due to Fe^{3+} impurities present in the glass.

In glass ceramic systems, it has been observed that the characteristic Cr^{3+} signals remain after the annealing [62,63]. Moreover, after the precipitation of lithium metasilicate crystalline phase in $65SiO_2$–$5Al_2O_3$–$26Li_2O$–$4K_2O$ composition glass ceramics, the Cr^{3+} signal intensity increases [63]. In combination with results of absorption spectra studies, it was concluded that Cr^{3+} ions occupy sites with octahedral symmetry in the lithium metasilicate crystal lattice [63].
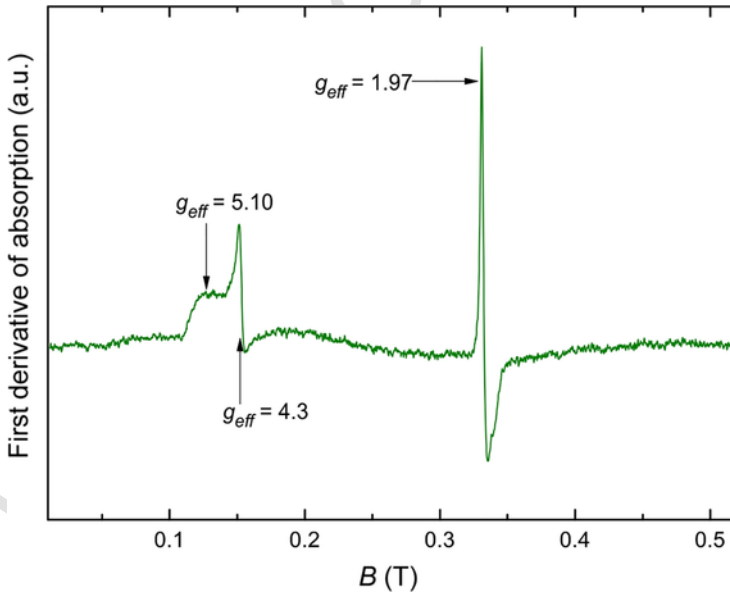
FIG. 12 EPR spectrum of a chromium doped glass sample (nominal composition: 46-SiO_2–$20Al_2O_3$–$8CaCO_3$–$26CaF_2$–$0.1Cr_2O_3$).

A study of persistent luminescence in $ZnGa_2O_4$ nanocrystals containing transparent glass ceramics revealed that the same types of Cr^{3+} defects are created as in microcrystalline $ZnGa_2O_4$ powders [64]. With an increasing annealing temperature, the EPR lines became narrower, indicating less disorder in the surrounding crystal field. From simulations with SH parameters used for $ZnGa_2O_4$ powders [65], five types of Cr^{3+} centers were identified, and their relative concentrations could be estimated from the double integral values of simulation curves [64].

8.3.5 Gd^{3+}

Contrary to most other rare earth ions, the $4f^7$ configuration S-state ions Gd^{3+} and Eu^{2+} have unusually long spin–lattice relaxation, which enables EPR investigations of these systems even at room temperature. As a consequence, Gd^{3+} centers in various hosts have been characterized quite extensively [66]. For the interpretation of $S = 7/2$ EPR spectra up to sixth order, ZFS terms must be included in the SH. HF structure is seldomly resolved in Gd^{3+} X-band EPR spectra measurements; therefore, the HF interaction term of Eq. (2) is usually neglected.

The $4f^7$ element X-band EPR spectra in glasses are remarkably similar to each other, sharing prominent features at $g_{eff} \approx 6.0$, 2.8 and 2.0. The spectrum is labeled as the "U-type" due to its ubiquity in vitreous and disordered materials [67–70]. Gd^{3+} and Eu^{2+} EPR spectra in oxyfluoride glasses are shown in Fig. 13. Mathematical simulations of the U-type spectrum reveal that a broad distribution of second order ZFS parameters is required for the reconstruction of the spectrum [67–69]. This can be explained on the basis that rare earth ions in glasses coordinate with a relatively large number of irregularly positioned ligands [69].

Given that ZFS of a $S = 7/2$ system is host sensitive, EPR spectroscopy in combination with Gd^{3+} paramagnetic probes is ideally suited to investigate the incorporation of trivalent rare earth ions in the crystalline phase of glass ceramics.

Studies of gadolinium local structure in $0.857Bi_2O_3$–$0.143GeO_2$ system reveal a tendency for forming Gd^{3+} clusters in the glassy phase of glass ceramics [71]. An asymmetric resonance observed at $g_{eff} \approx 4.3$, on the other hand, has been attributed to lower coordinated Gd^{3+} ions substituting Bi^{3+} ions in the developed crystalline phases of the material [71].
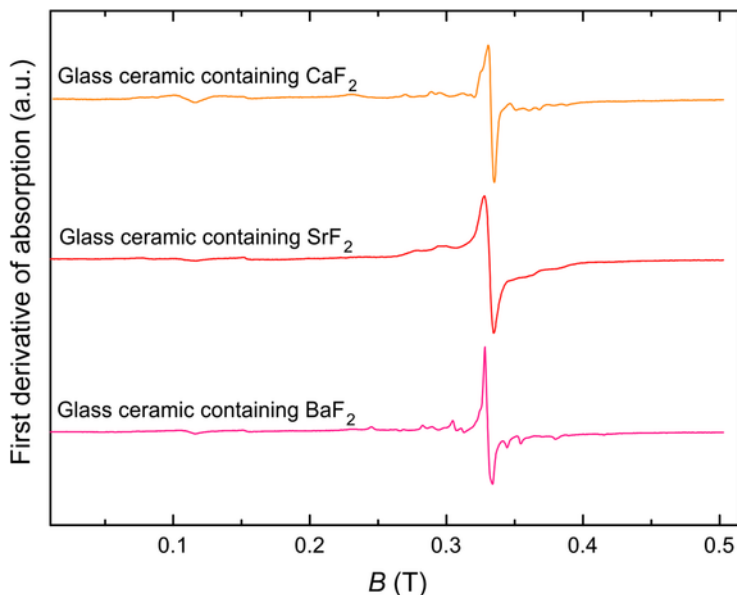
A number of gadolinium doped glass ceramic studies have reported that an intense resonance centered at $g_{eff} \approx 2.0$ overlays the U-type spectrum after the heat treatment of the precursor glass [43,47,72,73]. A g value of 1.992 is typical for Gd^{3+} centers in various symmetry single crystals [66]. Gd^{3+} EPR spectra of oxyfluoride glass ceramics containing CaF_2, SrF_2, and BaF_2 crystalline phases are shown in Fig. 14.
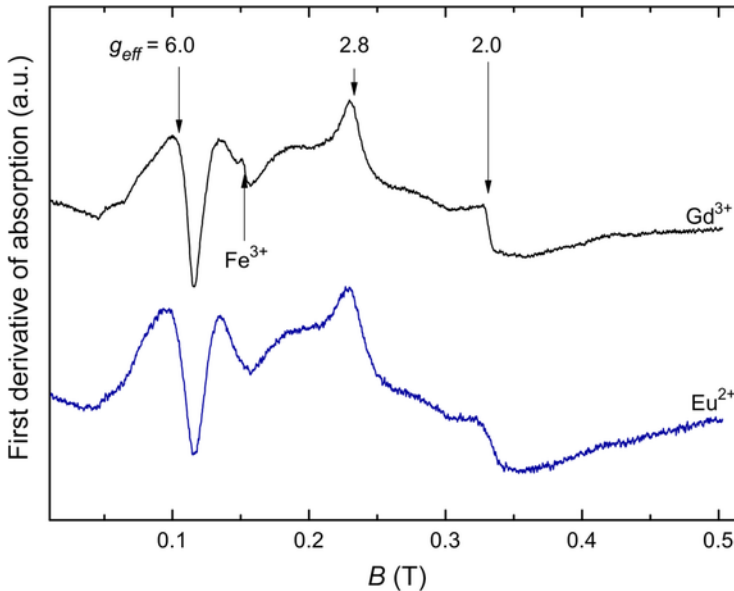
FIG. 13 EPR spectra of gadolinium ($40SiO_2$–$25Al_2O_3$–$15Na_2CO_3$–$20SrF_2$–$0.1GdF_3$) and europium ($50SiO_2$–$20Al_2O_3$–$10NaF$–$19SrF_2$–$1EuF_3$) doped glasses.

As visible from the spectra, ZFS peak positions as well as the line-widths are sensitive to the crystalline phase present in the glass ceramic. The former observation can be explained by different crystal fields around Gd^{3+} ions in the hosts of CaF_2, SrF_2, and BaF_2, whereas the latter is dependent on the Gd^{3+} ion distribution in the lattice—closer located paramagnetic centers will experience dipolar interaction induced EPR line broadening. More information can be obtained via EPR spectra simulations. Fig. 15 shows EPR spectra of oxyfluoride glass ceramic samples containing CaF_2 nanocrystals annealed at different temperatures, and the best correspondence spectra simulations with SH parameter sets are reported for single crystal CaF_2:Gd^{3+} [74].

Glass ceramics annealed at 700°C contain a rather symmetric signal with maximum at ≈ 0.33 T; however, after annealing the same composition at 800°C, another set of lines at lower magnetic fields emerges. This means that several sites are possible for trivalent rare earth ions in glass ceramics containing CaF_2, and their formation can be controlled by varying the thermal treatment parameters. Although the structure of cubic fluorite fluorides (CaF_2, SrF_2, BaF_2) is relatively simple, additional charge compensation is necessary when a trivalent ion substitutes the divalent cation in the lattice. Depending on the type of charge compensator as well as its orientation relative to the Gd^{3+} ion, several distinct gadolinium centers are possible [66,74]. The EPR spectrum of glass ceramics annealed at 700°C can be satisfactorily simulated using SH parameter values determined for the cubic CaF_2:Gd^{3+} center [74]. This in-

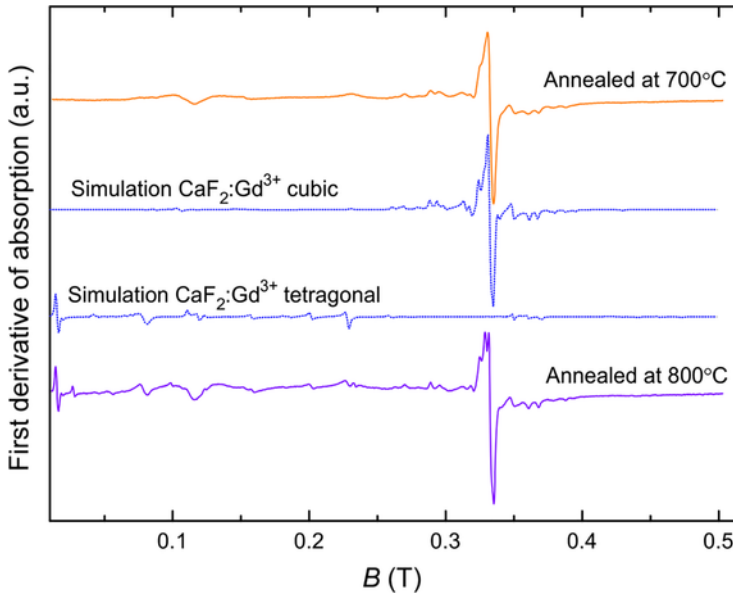**FIG. 14**   EPR spectra of gadolinium doped glass ceramics (nominal compositions from top to bottom: $46SiO_2–20Al_2O_3–8CaCO_3–26CaF_2–0.1Gd_2O_3$; $40SiO_2–25Al_2O_3–15Na_2CO_3–20SrF_2–GdF_3$; $62SiO_2–6Al_2O_3–15Na_2O–3NaF–14BaF_2–0.1GdF_3$).

dicates the formation of isolated cubic Gd^{3+} centers in the crystalline phase of glass ceramics in agreement with previous studies [72]. In order to maintain the cubic crystal field symmetry around Gd^{3+}, the charge compensator must be located outside its first coordination spheres. Annealing at higher temperatures produces another type of gadolinium center—a tetragonal symmetry $CaF_2:Gd^{3+}$ center. Similar effects in the formation of cubic and tetragonal symmetry Gd^{3+} centers have also been observed in oxyfluoride glass ceramics containing SrF_2 crystalline phase [73]. On the other hand, in-glass ceramics containing BaF_2 crystalline phase only trigonal symmetry fluorine ion compensated Gd^{3+} centers have been observed [73]. The size mismatch between Ba^{2+} (149 pm) and Gd^{3+} (108 pm) ions is greater than for Ca^{2+} (114 pm) and Sr^{2+} (132 pm) ions [75]; therefore, more significant local structure distortions are expected for Gd^{3+} substitution defects in BaF_2 [73].

Spontaneous crystallization during the melt-quenching process is also possible when preparing glass ceramics. This process is influenced by the chosen composition as well as the cooling rate of the sample. For example, compositions rich in fluorine content tend to undergo phase separation during the melting, which provide nucleation centers for fluoride phases and enable rapid crystal growth in the glasses. The effect of spontaneous crystallization is usually estimated from XRD or TEM data; however, as shown in Fig. 16, it can be also seen from Gd^{3+} paramagnetic probe EPR spectra. The X-ray amor-
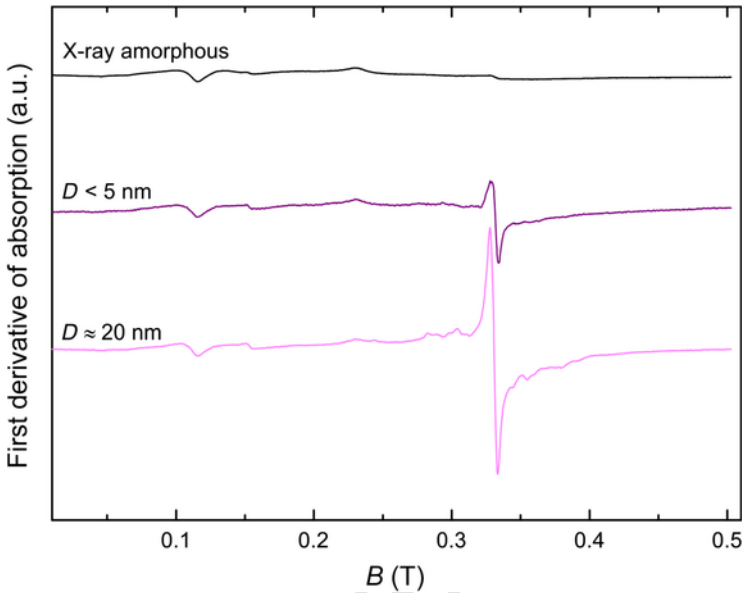
FIG. 15   EPR spectra of gadolinium doped glass ceramics (nominal composition: 46-SiO_2–20Al_2O_3–8$CaCO_3$–26CaF_2–0.1Gd_2O_3). Simulations with CaF_2:Gd^{3+} center SH parameters from Ref. [74].

phous sample exhibits the signature Gd^{3+} U-type spectrum. EPR spectrum of a sample containing ultra-small (< 5 nm) nanoparticles has an additional structure-less Gaussian peak at $g_{eff} \approx 2$. A significantly crystallized glass ceramic sample where the initial nanoparticle size is ≈ 20 nm has a more intense crystalline phase signal with better resolved fine structure. The average crystallite size has been estimated from Eq. (1).

Rapid quenching is a non-equilibrium process and for defect centers formed this way deviations from Gd^{3+} centers observed in single crystals could be expected. Fig. 17 shows EPR spectra of the above-illustrated "self-crystallized" glass ceramic sample with ≈ 20 nm large BaF_2 nanocrystals, samples thermally treated afterward, and a simulation with trigonal BaF_2:Gd^{3+} SH parameters from Ref. [76]. There is a wide envelope curve superimposing the trigonal BaF_2:Gd^{3+} EPR spectrum in the initial sample. It could be explained by the incorporation of Gd^{3+} ions in slightly different local environments in BaF_2 nanocrystals producing a distribution of ZFS parameter values. Thus, it is evident that post-quenching thermal treatment of a self-crystallized sample is required to form the isolated gadolinium centers characteristic for the respective single crystal.

The phenomenon of "self-crystallization" in lead tellurite and zinc borate glass ceramics has been found to correlate with the content of Gd_2O_3 in the initial composition [77,78]. In these studies, magnetic susceptibility measure-

FIG. 16 EPR spectra of gadolinium doped as prepared "glasses" with varying degree of crystallization (nominal compositions from *top* to *bottom*: $50SiO_2–20Al_2O_3–10NaF–20SrF_2–0.1GdF_3$; $40SiO_2–25Al_2O_3–15Na_2CO_3–20SrF_2–0.1GdF_3$; $62-SiO_2–6Al_2O_3–15Na_2O–3NaF–14BaF_2–0.1GdF_3$).

ments in combination with EPR have been employed to analyze the structure details of the Gd^{3+} local environment. If the gadolinium content in the composition is relatively low, Gd^{3+} ions are randomly distributed in the glass matrix forming isolated centers. At higher doping concentrations, clustering of gadolinium is observed, and the formation of super-exchange coupled $Gd^{3+}–O–Gd^{3+}$ pairs occurs [78].

8.3.6 Eu^{2+}

Europium ions can be found in two stable valence states—3 + and 2 +, which differ drastically by their spectroscopic and magnetic properties. Eu^{3+} ions have characteristic narrow-line luminescence in the red spectral region, whereas optical spectra of Eu^{2+} consist of wide bands that are sensitive to the surrounding ligand field. It is fascinating to note that due to the absence of one electron in comparison to Eu^{2+}, the ground state of Eu^{3+} is rendered diamagnetic and, as, a consequence, it is not detectable via EPR spectroscopy. The electron configuration of Eu^{2+}, on the other hand, is the same as for $Gd^{3+}–4f^7$. Thus, first and foremost, EPR investigations of europium-doped systems, including glass ceramics, allow to detect the valence state of activators.

As shown above in Fig. 13, EPR spectra of Eu^{2+} in glasses are strikingly similar to Gd^{3+}, sharing the characteristic resonances of the U-type spectrum.
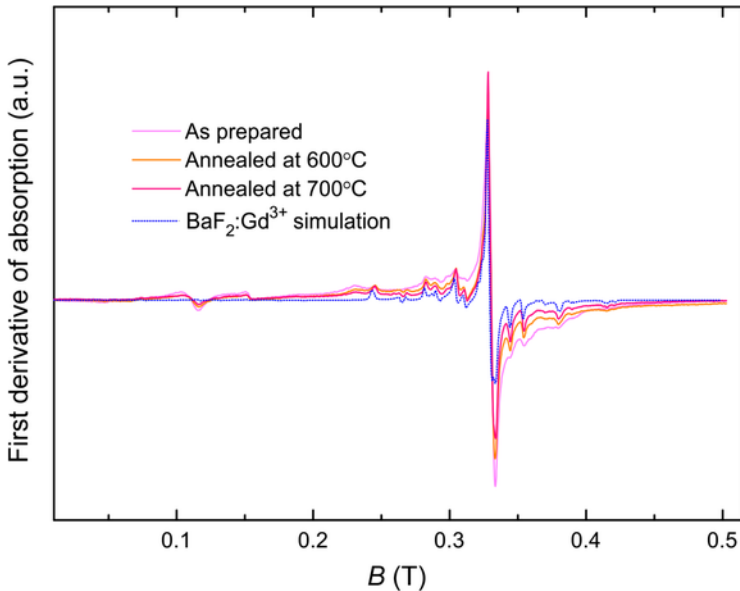
FIG. 17 EPR spectra evolution of a gadolinium doped self-crystallized glass ceramic upon thermal treatment (nominal composition: $62SiO_2$–$6Al_2O_3$–$15Na_2O$–$3NaF$–$14BaF_2$–$0.1GdF_3$). Simulation with trigonal BaF_2:Gd^{3+} center SH parameters from Ref. [76].

Several differences are to be expected in typical Eu^{2+} spectra, though:

- Nuclear magnetic moments of europium isotopes are approximately an order of magnitude greater than those of gadolinium; therefore, the HF interaction effects are usually detected in X-band EPR spectra.

- The magnitude of the HF splitting of the stable ^{151}Eu ($I = 5/2$; $g_n = 1.389$; 48% abundant) and ^{153}Eu ($I = 5/2$; $g_n = 0.6134$; 52% abundant) isotopes characterized by the A value are determined by the nuclear g_n factor of the isotope. Thus, each of the fine structure lines is split into two sets of $2I + 1 = 6$ components.

- Systems, where europium is present in both valence states, will produce less pronounced spectra as only the paramagnetic Eu^{2+} ions can contribute to the total EPR spectrum intensity.

Incorporation of Eu^{2+} ions in $BaBr_2$ single crystals and fluorobromozirconate glass ceramics containing $BaBr^{2+}$ have been investigated [79]. The glass ceramic EPR spectrum qualitatively shared the main features as the calculated $BaBr_2$:Eu^{2+} powder spectrum leading to the conclusion that Eu^{2+} is incorporated in the $BaBr_2$ crystalline phase of the material. It was proposed that centers experience deviations in SH parameters to account for the broader spectra features of glass ceramics [79].

A number of studies have been devoted to the investigation of $Eu^{3+} \rightarrow Eu^{2+}$ reduction phenomenon in oxyfluoride glasses and glass ceramics containing MeF_2 (Me = Ca, Sr, Ba) [80–84]. In glasses, the increase of fluorine anion content in the composition has been observed to enhance the conversion to Eu^{2+} [80]. In systems where CaF_2 nanocrystals were formed during the melt-quenching process, the conversion efficiency with increased self-crystallization also improved [81]. Precipitation of SrF_2 nanocrystals during thermal treatment of the precursor glass has also promoted the reduction to Eu^{2+} [82,83]. The effect was observed from the increase of broad Eu^{2+} photoluminescence band in the blue spectral region; however, as both oxyfluoride glasses and SrF_2 crystals typically have blue Eu^{2+} photoluminescence spectra, it was not possible to determine conclusively whether Eu^{2+} ions actually incorporate the crystalline phase. The incorporation of Eu^{2+} in the BaF_2 crystalline phase of glass ceramics after thermal treatment has been justified on the basis of the charge compensation model [84]. EPR spectroscopy in these studies could have been an extremely useful tool to providing direct experimental evidence of the local surroundings around Eu^{2+} ions.

The effects of sample composition and annealing conditions on the valence state and local structure of europium ions via EPR spectroscopy have been investigated in SrF_2 containing glass ceramics [85]. In samples with increased fluorine content, SrF_2 nanoparticles with the average size of ≈ 10 nm were formed during the melt-quenching process. These samples also exhibited broad blue emission; however, EPR measurements detected that Eu^{2+} ions reside in a disordered environment, not SrF_2 nanocrystals, as could be expected. The "self-crystallization" effect upon decreasing the fluorine content was diminished, and europium in the 3 + state was dominant. $Eu^{3+} \rightarrow Eu^{2+}$ conversion was not efficient after annealing at a temperature (650°C) where SrF_2 nanocrystals were formed, therefore, mainly Eu^{3+} ions incorporated into the high symmetry environment. The increase of annealing temperature to 800°C significantly enhanced the reduction process, and both photoluminescence and EPR analysis indicated the presence of Eu^{2+} ions in complex silicate structures [85]. EPR spectra samples containing europium annealed at 650°C and 800°C are shown in Figs. 18 and 19 respectively.

The EPR spectrum in Fig. 18 contains a vague signal of weak narrow lines superimposing a broad Gaussian curve similar to what was observed in polycrystalline SrF_2:Eu^{2+} [85]. Envelope curves probably originating from Eu^{2+} in disordered environment are also present. A quick comparison with the EPR signal-to-noise ratio of similar systems containing Gd^{3+} (e.g., Fig. 14) indicates that a relatively low number of isolated SrF_2:Eu^{2+} centers is present in the glass ceramic sample.

Eu^{2+} EPR spectrum features in Fig. 19 are much better resolved. In this case, ZFS is ≈ 0, and the complex structure has been satisfactorily simulated in a $S = 7/2$ model and HF interaction with europium isotopes ^{151}Eu and ^{153}Eu. Furthermore, the ratio of the HF parameters $A(^{151}Eu)/A(^{153}Eu)$ corresponds
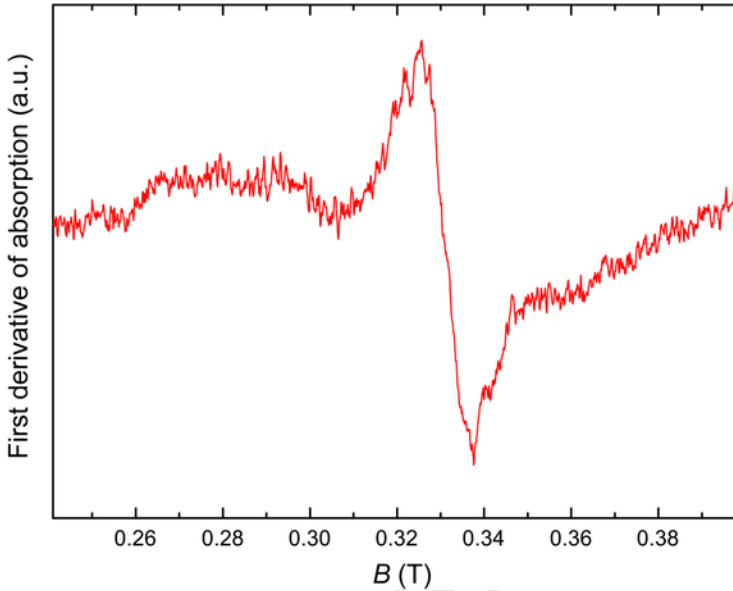
FIG. 18 EPR spectrum of europium doped glass ceramic after annealing at 650°C (nominal composition: $40SiO_2$–$25Al_2O_3$–$15Na_2CO_3$–$19SrF_2$–$1EuF_3$).

well with the ratio of nuclear g_n factors $g_n(^{151}Eu)/g_n(^{153}Eu) = 2.26$ [85]. The relative intensities of the two signals are determined by the natural abundances of the isotopes. The increased EPR signal intensity suggests that the $Eu^{3+} \rightarrow Eu^{2+}$ reduction process in oxyfluoride glass ceramics is more efficient at higher annealing temperatures.

8.3.7 Er^{3+}

Erbium-doped glass ceramics have received a considerable scientific and practical interest due to the ladder-like energy level arrangements, which can enable infrared radiation up-conversion to visible light [9–19]. The up-conversion process can be orders of magnitude more efficient if Er^{3+} ions incorporate the developed crystalline phases of the glass ceramic material. In EPR spectra analysis, the $4f^{11}$ configuration is approximated as a $S = 1/2$ system. Satellite lines caused by the HF interaction with the 23% naturally abundant ^{167}Er isotope with $I = 7/2$ are typically resolved in Er^{3+} spectra. A major setback from the viewpoint of magnetic resonance investigations is the short spin–lattice relaxation time of Er^{3+}, which manifests itself in the need for low temperatures (< 30K) for EPR spectra detection.

The necessity of ultra-low temperatures has hindered EPR investigations of Er^{3+} in glasses; therefore, not as much data as for the S-state rare earth ions
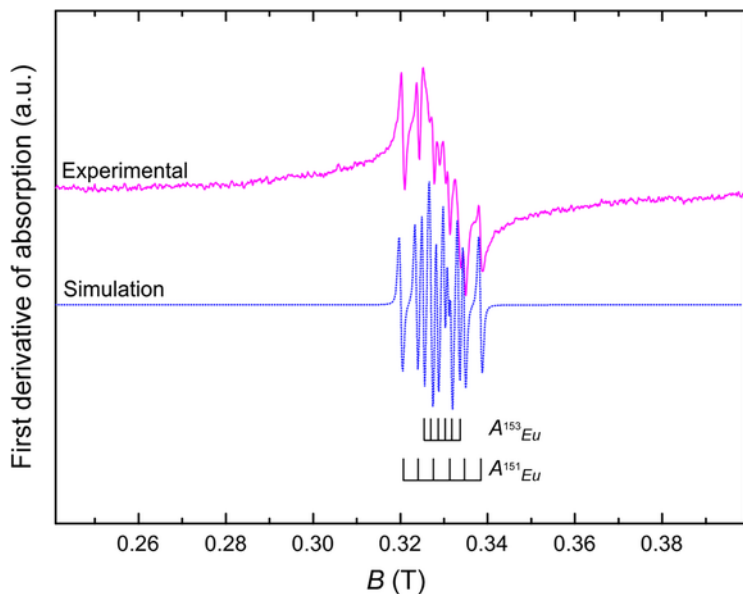
FIG. 19   EPR spectrum of europium doped glass ceramic after annealing at 800°C (nominal composition: $40SiO_2$–$25Al_2O_3$–$15Na_2CO_3$–$19SrF_2$–$1EuF_3$). Simulation with Eu^{2+} center SH parameters from Ref. [85].

Gd^{3+} and Eu^{2+} have been reported. In the existing EPR studies of Er^{3+} ions in glasses, broad features at low magnetic fields have been observed [86–88].

In erbium-doped $25GeS_2$–$35Ga_2S_3$–$40CsCl$ chalcogenide glass ceramics, no additional EPR spectra features were observed upon the crystallization of Ga_2S_3 crystals. The intensity increase of the broad band located at $g_{eff} \approx 5.15$ indicated that the surrounding environment of Er^{3+} is modified by the crystallization process [87].

In oxyfluoride glass ceramics containing fluorite structure β-PbF_2 crystalline phase, the segregation of Er^{3+} in the crystallites was almost complete. In nanocrystals, the cubic Er^{3+} environment in glass ceramics was identified by the almost identical SH values previously determined in PbF_2:Er^{3+} single crystals [88].

Incorporation of Er^{3+} in a cubic environment of the CaF_2 crystalline phase has been reported in oxyfluoride glass ceramics [89]. In this particular study, the EPR signal was detected optically on a magnetic circular dichroism (MCD) band. Optical detection of paramagnetic activators is especially advantageous for a direct and unambiguous attribution of optical properties to paramagnetic center local structure [90]. The MCD-EPR technique has been applied previously to detect cubic CaF_2:Gd^{3+} centers as well [72]. It would be interesting to determine whether Er^{3+} embed lower symmetry environments in CaF_2 nanocrystals after annealing at higher temperatures as is the case of

Gd^{3+} impurities shown in Fig. 15. The drawback of the MCD-EPR technique is the requirement of transparent samples; therefore, significantly crystallized glass ceramics obtained at higher temperatures cannot be studied this way.

Simulations of the expected CaF_2:Er^{3+} X-band EPR signals in glass ceramics are shown in Fig. 20. Only the 23% of Er^{3+} centers bound to the ^{167}Er nucleus experience splitting into the 8 component HF structure. The A values in [91] have been reported only for the cubic CaF_2:Er^{3+} center.

8.3.8 Yb^{3+}

Yb^{3+} is a $4f^{13}$ configuration paramagnetic ion with $S = 1/2$. The magnetic nuclear isotopes of ytterbium are ^{171}Yb ($I = 1/2$; 14% abundant) and ^{173}Yb ($I = 5/2$; 16% abundant). Similarly to Er^{3+}, the spin–lattice relaxation time at room temperature is very short; therefore, low temperatures are a prerequisite for Yb^{3+} paramagnetic center EPR detection.

Yb^{3+} spectra in glasses are usually analyzed by assuming an axial symmetry SH (see Eq. 5). The determination of the precise g-tensor components $g_{\perp}$ and $g_{\parallel}$ is problematic due to the inhomogeneous broadening of the spectra. Variations in the parameter values reflect the different environments around Yb^{3+} ions. EPR spectra features exceeding the theoretical maximal value of $g_{eff} \approx 8$ for isolated Yb^{3+} centers have been assigned to ytterbium ion pairs and clusters [86,92,93].
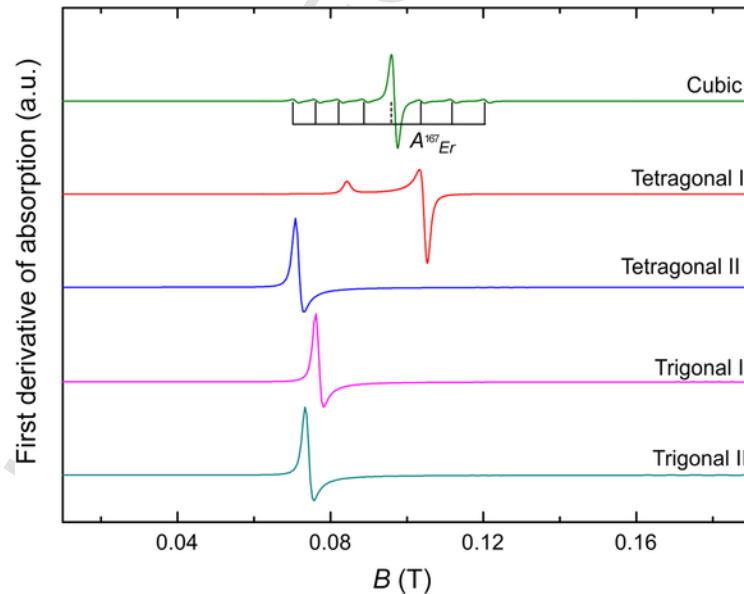

FIG. 20 Simulations of EPR spectra corresponding to various symmetry centers in polycrystalline CaF_2:Er^{3+} with SH parameters from Ref. [91].

In oxyfluoride glass ceramics containing β-PbF_2 crystallites, complete incorporation of Yb^{3+} ions in the crystalline phase was observed during the devitrification process [94]. Furthermore, optical properties of the investigated glass ceramics were similar to the counterpart single crystals making the material potentially interesting for laser applications. A simulation of the observed signal in Ref. [94] is shown in Fig. 21.

8.3.9 Other paramagnetic centers

Fe^{3+} ions are often observed as impurities in different materials (see, for example, the resonance at $g_{eff} \approx 4.3$ in Figs. 12 and 13); however, there is little information about iron-doped glass ceramics. Fe^{3+} electron configuration $3d^5$ is the same as for Mn^{2+}, yet EPR spectra are distinctly different due the lack of well-defined HF structure. Thus, Fe^{3+} EPR spectra features in glasses can be explained by variations of second order ZFS parameters [34]. In iron-doped calcium borophosphate glass ceramics, supplementary line at $g_{eff} \approx 6$ was observed after the thermal treatment; however its intensity relative to the central resonance at $g_{eff} \approx 2$ already present in the precursor glass sample was negligible [95].

In Te- and Bi-doped glasses and glass ceramics, several types of EPR signals have been observed—Fe^{3+} impurity signals as well as possible molecular ions of Te_2^{-} and Bi_2^{-} [96]. The role of titanium ions on the physical and
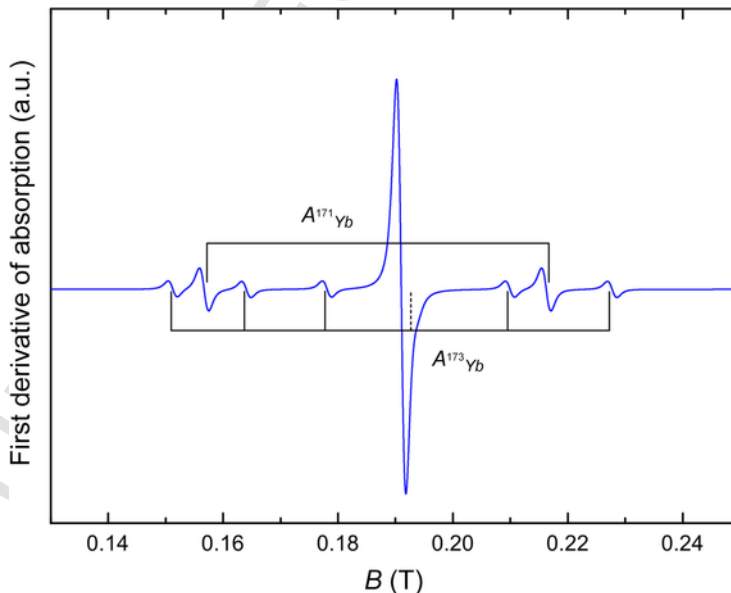
FIG. 21 Simulation of PbF_2:Yb^{3+} center EPR spectrum observed in oxyfluoride glass ceramics [94].

structural properties of calcium zinc bismuth phosphate glass ceramics has been investigated. Ti^{3+} ions were found to occupy tetragonally distorted octahedral sites possibly weakening the glass ceramic network [97].

Glass ceramic materials could be potentially used in scintillator applications [98]; therefore, characterization of radiation-induced paramagnetic centers could also be of interest in these systems. EPR spectra of X-ray-induced radiation defects have been observed in lithium oxyfluoride glass ceramics [99]. The observed signal could be explained within a model of an F-type center in the YF_3 crystalline phase present in the material on the basis of EPR spectrum HF structure [99].

The industrial demand for novel materials requires a profound understanding on how specific properties can be tuned by modifying material's structure and introducing defects. The EPR method offers a great diversity of ways to complement other spectroscopic techniques in the characterization of point defects such as providing the detection of paramagnetic impurity ions or the valence state of activators in the material. Glass ceramic investigations additionally benefit from the high EPR spectra sensitivity to the local environment around the defect site, which enables to determine, whether activator ions reside in the amorphous phase or incorporate in the crystalline phases. It would be interesting to investigate the effects of activator local structure disorder due to the nano-size of crystallites in more detail. Quantitative EPR analysis methods for the evaluation of paramagnetic center distribution in the different sites of glass ceramics could also be utilized more in the future.

ACKNOWLEDGMENTS

REFERENCES

[1] D. Chen, W. Xiang, X. Liang, J. Zhong, H. Yu, M. Ding, et al., Advances in transparent glass–ceramic phosphors for white light-emitting diodes—a review, J. Eur. Ceram. Soc. 35 (2015) 859–869, https://doi.org/10.1016/j.jeurceramsoc.2014.10.002.

[2] P. Babu, K.H. Jang, C.S. Rao, L. Shi, C.K. Jayasankar, V. Lavín, et al., White light generation in Dy^{3+}-doped oxyfluoride glass and transparent glass-ceramics containing CaF_2 nanocrystals, Opt. Express 19 (2011) 1836, https://doi.org/10.1364/OE.19.001836.

[3] C.R. Li, S.F. Li, Y.Y. Guo, X.Y. Zhou, J.C. Sun, Y. Song, et al., White light emission of Dy^{3+}-doped and Dy^{3+}:Yb^{3+}-codoped oxyfluoride glass ceramics under 388-nm excitation, J. Mod. Opt. 62 (2015) 1638–1642, https://doi.org/10.1080/09500340.2015.1061060.

[4] Z. Zhang, Y. Zhang, Z. Feng, W. Cheng, H. Xia, X. Zhang, Luminescent properties of Ce^{3+}/Tb^{3+} co-doped glass ceramics containing YPO_4 nanocrystals for W-LEDs, J. Rare Earths 34 (2016) 464–469, https://doi.org/10.1016/S1002-0721(16)60050-9.

[5] L.Q. Yao, G.H. Chen, H.J. Zhong, S.C. Cui, F. Li, J.Y. Gan, Enhanced luminescent properties in Tm^{3+}/Dy^{3+} transparent phosphate glass ceramic, MATEC Web Conf. 67 (2016) 1-6.

[6] R. Bagga, V. Gopal, A. Goel, J.M.F. Ferreira, N. Pal, P. Singh, et al., Nanocrystals for white light generation, Mater. Sci. Eng. B 178 (2013) 218–224, https://doi.org/10.1016/j.mseb.2012.10.023.

[7] M. Kemere, J. Sperga, U. Rogulis, G. Krieke, J. Grube, Luminescence properties of Eu, RE^{3+} (RE = Dy, Sm, Tb) co-doped oxyfluoride glasses and glass–ceramics, J. Lumin. 181 (2017) 25–30, https://doi.org/10.1016/j.jlumin.2016.08.062.

[8] M. Kemere, U. Rogulis, J. Sperga, Luminescence and energy transfer in Dy^{3+}/Eu^{3+} co-doped aluminosilicate oxyfluoride glasses and glass-ceramics, J. Alloys Compd. 735 (2018) 1253–1261, https://doi.org/10.1016/j.jallcom.2017.11.077.

[9] D. Chen, Y. Zhou, Z. Wan, P. Huang, H. Yu, H. Lu, et al., Enhanced upconversion luminescence in phase-separation-controlled crystallization glass ceramics containing Yb/Er(Tm): $NaLuF_4$ nanocrystals, J. Eur. Ceram. Soc. 35 (2015) 2129–2137, https://doi.org/10.1016/j.jeurceramsoc.2015.01.021.

[10] G. Krieke, A. Sarakovskis, Crystallization and upconversion luminescence of distorted fluorite nanocrystals in Ba^{2+} containing oxyfluoride glass ceramics, J. Eur. Ceram. Soc. 36 (2015) 1715–1722, https://doi.org/10.1016/j.jeurceramsoc.2016.01.025.

[11] A. Sarakovskis, G. Krieke, Upconversion luminescence in erbium doped transparent oxyfluoride glass ceramics containing hexagonal $NaYF_4$ nanocrystals, J. Eur. Ceram. Soc. 35 (2015) 3665–3671, https://doi.org/10.1016/j.jeurceramsoc.2015.06.014.

[12] G. Krieke, A. Sarakovskis, M. Springis, Cubic and rhombohedral $Ba_4Lu_3F_{17}:Er^{3+}$ in transparent glass ceramics: crystallization and upconversion luminescence, J. Lumin. 200 (2018) 265–273, https://doi.org/10.1016/j.jlumin.2018.04.016.

[13] Y. Kawamoto, R. Kanno, J. Qiu, Upconversion luminescence of Er^{3+} in transparent $SiO_2–PbF_2–ErF_3$ glass ceramics, J. Mater. Sci. 3 (1998) 63, https://doi.org/10.1023/A:1004333310532.

[14] G. Krieke, A. Sarakovskis, M. Springis, Upconversion luminescence of Er^{3+}/Yb^{3+} and their role in the stabilization of cubic $NaLaF_4$ nanocrystals in transparent oxyfluoride glass ceramics, J. Non-Cryst. Solids 481 (2018) 335–343, https://doi.org/10.1016/j.jnoncrysol.2017.11.016.

[15] F. Liu, E. Ma, D. Chen, Y. Yu, Y. Wang, Tunable red-green upconversion luminescence in novel transparent glass ceramics containing Er: $NaYF_4$ nanocrystals, J. Phys. Chem. B 110 (2006) 20843–20846, https://doi.org/10.1021/jp063145m.

[16] X. Qiao, X. Fan, J. Wang, M. Wang, Luminescence behavior of Er^{3+} ions in glass-ceramics containing CaF_2 nanocrystals, J. Non-Cryst. Solids 351 (2005) 357–363, https://doi.org/10.1016/j.jnoncrysol.2004.11.021.

[17] J. Cai, X. Wei, F. Hu, Z. Cao, L. Zhao, Y. Chen, et al., Up-conversion luminescence and optical thermometry properties of transparent glass ceramics containing $CaF_2:Yb^{3+}/Er^{3+}$ nanocrystals, Ceram. Int. 42 (2016) 13990–13995, https://doi.org/10.1016/j.ceramint.2016.06.002.

[18] F. Hu, Z. Zhao, F. Chi, X. Wei, M. Yin, Structural characterization and temperature-dependent luminescence of $CaF_2:Tb^{3+}/Eu^{3+}$ glass ceramics, J. Rare Earths 35 (2017) 536–541, https://doi.org/10.1016/S1002-0721(17)60945-1.

[19] W. Xu, X. Gao, L. Zheng, Z. Zhang, W. Cao, An optical temperature sensor based on the upconversion luminescence from Tm^{3+}/Yb^{3+} codoped oxyfluoride glass ceramic, Sens. Actuators B 173 (2012) 250–253, https://doi.org/10.1016/j.snb.2012.07.009.

[20] P.P. Fedorov, A.A. Luginina, A.I. Popov, Transparent oxyfluoride glass ceramics, J. Fluor. Chem. 172 (2015) 22–50, https://doi.org/10.1016/j.jfluchem.2015.01.009.

[21] A. Tressaud, Functionalized Inorganic Fluorides: Synthesis, Characterization and Properties of Nanostructured Solids, John Wiley & Sons, 2010 https://doi.org/10.1002/9780470660768.

[22] N. Karpukhina, R.G. Hill, R.V. Law, Crystallisation in oxide glasses—a tutorial review, Chem. Soc. Rev. 43 (2014) 2174, https://doi.org/10.1039/c3cs60305a.

[23] A.J. Stevenson, H. Serier-Brault, P. Gredin, M. Mortier, Fluoride materials for optical applications: single crystals, ceramics, glasses, and glass-ceramics, J. Fluor. Chem. 132 (2011) 1165–1173, https://doi.org/10.1016/j.jfluchem.2011.07.017.

[24] R.H. Doremus, Glass Science, John Wiley and Sons, New York, 1994.

[25] V. Marghussian, Nano-Glass Ceramics: Processing, Properties and Applications, William Andrew, 2015 https://doi.org/10.1016/C2014-0-01294-4.

[26] W. Höland, G.H. Beall, Glass-Ceramic Technology, NJ: Wiley, 2012 https://doi.org/10.1002/9781118265987.

[27] A. Monshi, M.R. Foroughi, M.R. Monshi, Modified Scherrer equation to estimate more accurately nano-crystallite size using XRD, World J. Nano Sci. Eng. 2 (2012) 154–160, https://doi.org/10.4236/wjnse.2012.23020.

[28] C. Rudowicz, M. Karbowiak, Disentangling intricate web of interrelated notions at the interface between the physical (crystal field) Hamiltonians and the effective (spin) Hamiltonians, Coord. Chem. Rev. 287 (2015) 28–63, https://doi.org/10.1016/j.ccr.2014.12.006.

[29] A. Abragam, B. Bleaney, Electron Paramagnetic Resonance of Transition Ions, Clarendon Press, 1970https://doi.org/10.1017/CBO9781107415324.004.

[30] J.A. Weil, J.R. Bolton, Electron Paramagnetic Resonance, Wiley, 2007.

[31] G.R. Eaton, S.S. Eaton, D.P. Barr, R.T. Weber, Quantitative EPR, Springer, 2010.

[32] S.K. Misra, Multifrequency Electron Paramagnetic Resonance: Theory and Applications, Wiley, 2011https://doi.org/10.1002/9783527633531.

[33] M. Brustolon, E. Giamello, Electron Paramagnetic Resonance: A Practitioner's Toolkit, Wiley, 2008https://doi.org/10.1002/9780470432235.

[34] D.L. Griscom, Electron spin resonance in glasses, J. Non-Cryst. Solids 40 (1980) 211–272, https://doi.org/10.1016/0022-3093(80)90105-2.

[35] S. Stoll, A. Schweiger, EasySpin, a comprehensive software package for spectral simulation and analysis in EPR, J. Magn. Reson. 178 (2006) 42–55.

[36] D.L. Griscom, Electron spin resonance, In: in: D.R. Uhlmann, N.J. Kreidl (Eds.), Glass Science and Technology, Elsevier,, 1990, pp. 151–251.

[37] J.M. Dance, J.J. Videau, J. Portier, EPR of transition metal ions (Mn^{2+}, Cu^{2+}, Cr^{3+}, Fe^{3+}) in fluoroaluminate glasses, J. Non-Cryst. Solids 86 (1986) 88–93, https://doi.org/10.1016/0022-3093(86)90478-3.

[38] A. Drzewiecki, B. Padlyak, V. Adamiv, Y. Burak, I. Teslyuk, EPR spectroscopy of Cu^{2+} and Mn^{2+} in borate glasses, Nukleonika 58 (2013) 379–385 http://yadda.icm.edu.pl/yadda/element/bwmeta1.element.baztech-d47b5e67-a8e5-43d7-b2a2-0e390717aace.

[39] J. Kliava, EPR of impurity ions in disordered solids, Phys. Status Solidi B 134 (1986) 411–455, https://doi.org/10.1002/pssb.2221340202.

[40] J. Kliava, J. Purans, Simulation of EPR spectra of Mn^{2+} in glasses, J. Magn. Reson. 40 (1980) 33–45, https://doi.org/10.1016/0022-2364(80)90227-9.

[41] J. Purāns, J. Kliava, I. Millere, Computer simulation of Mn^{2+} EPR spectra in glasses with $g_{ef} = 4.29$, Phys. Status Solidi 56 (1979) 5–8, https://doi.org/10.1002/pssa.2210560152.

[42] W. Gehlhoff, W. Ulrici, Transition metal ions in crystals with the fluorite structure, Phys. Status Solidi 102 (1980) 11–59, https://doi.org/10.1002/pssb.2221020102.

[43] R.W.A. Franco, J.F. Lima, C.J. Magon, J.P. Donoso, Y. Messaddeq, Magnetic resonance study of the crystallization behavior of InF_3-based glasses doped with Cu^{2+}, Mn^{2+} and Gd^{3+}, J. Non-Cryst. Solids 352 (2006) 3414–3422, https://doi.org/10.1016/j.jnoncrysol.2006.02.107.

[44] A.R. Molla, R.P.S. Chakradhar, C.R. Kesavulu, J.L. Rao, S.K. Biswas, Microstructure, mechanical, EPR and optical properties of lithium disilicate glasses and glass-ceramics doped with Mn^{2+} ions, J. Alloys Compd. 512 (2012) 105–114, https://doi.org/10.1016/j.jallcom.2011.09.031.

[45] T. Satyanarayana, M.A. Valente, G. Nagarjuna, N. Veeraiah, Spectroscopic features of manganese doped tellurite borate glass ceramics, J. Phys. Chem. Solid 74 (2013) 229–235, https://doi.org/10.1016/j.jpcs.2012.09.011.

[46] F.J. Owens, Paramagnetic resonance of divalent manganese in thallous azide, J. Chem. Phys. 57 (1972) 118–126.

[47] A. Antuzevics, U. Rogulis, A. Fedotovs, A.I. Popov, Crystalline phase detection in glass ceramics by EPR spectroscopy, Low Temp. Phys. 44 (2018) 449–454.

[48] A. Fedotovs, D. Berzins, A. Sarakovskis, U. Rogulis, G. Doke, EPR studies of the oxyfluoride glass ceramics using Mn^{2+} as a paramagnetic probe, IOP Conf. Ser. Mater. Sci. Eng. 15 (2010) 12068, https://doi.org/10.1088/1757-899X/15/1/012068.

[49] A. Fedotovs, D. Berzins, O. Kiselova, A. Sarakovskis, Characteristics of the Mn^{2+} EPR spectra in the oxyfluoride glass ceramics containing SrF_2 nanocrystals, IOP Conf. Ser. Mater. Sci. Eng. 38 (2012) 12047, https://doi.org/10.1088/1757-899X/38/1/012047.

[50] D. Berzins, A. Fedotovs, O. Kiselova, A. Sarakovskis, EPR spectra of the Mn^{2+} ion in the oxyfluoride glass ceramics containing BaF_2 nanocrystalline phase, IOP Conf. Ser. Mater. Sci. Eng. 38 (2012) 12046, https://doi.org/10.1088/1757-899X/38/1/012046.

[51] S. Prakash Singh, R.P.S. Chakradhar, J.L. Rao, B. Karmakar, Electron paramagnetic resonance, optical absorption and photoluminescence properties of Cu^{2+} ions in $ZnO–Bi_2O_3–B_2O_3$ glasses, J. Magn. Magn. Mater. 346 (2013) 21–25, https://doi.org/10.1016/j.jmmm.2013.07.007.

[52] A. Hameed, G. Ramadevudu, M. Shareefuddin, M.N. Chary, EPR and optical absorption by Cu^{2+} ions in $ZnO–Li_2O–Na_2O–K_2O–B_2O_3$ glasses, AIP Conf. Proc. 1591 (2014) 842–844, https://doi.org/10.1063/1.4872775.

[53] A. Bhogi, P. Kistaiah, Structural and optical properties of CuO doped lithium borate glasses, Phys. Chem. Glasses Eur. J. Glass Sci. Technol. B 56 (2015) 197–202, https://doi.org/10.13036/17533562.56.5.197.

[54] I.D.A. Silva, J.P. Donoso, C.J. Magon, C.E. Tambelli, S.H. Santagneli, S.J.L. Ribeiro, et al., Magnetic resonance and conductivity study of lead-cadmium fluorosilicate glasses and glass-ceramics, J. Phys. Chem. C 122 (2018) 6288–6297, https://doi.org/10.1021/acs.jpcc.7b11517.

[55] M. Samdani, G. Ramadevudu, M. Narasimha Chary, M. Shareefuddin, EPR, optical and physical studies on Cr^{3+} doped $MgO–BaO–B_2O_3–TeO_2$ glasses, St. Petersbg. Polytech. Univ. J. Phys. Math. 3 (2017) 299–307, https://doi.org/10.1016/j.spjpm.2017.10.001.

[56] I. Ardelean, S. Filip, EPR and magnetic investigations of chromium ions in TeO_2 based glasses, J. Optoelectron. Adv. Mater. 7 (2005) 745–752.

[57] F.S. De Vicente, F.A. Santos, B.S. Simões, S.T. Dias, M.S. Li, EPR, optical absorption and luminescence studies of Cr^{3+}-doped antimony phosphate glasses, Opt. Mater. 38 (2014) 119–125, https://doi.org/10.1016/j.optmat.2014.10.012.

[58] M. Haouari, H. Ben Ouada, H. Maaref, H. Hommel, A.P. Legrand, Optical absorption and electron paramagnetic resonance study of Cr^{3+}-doped phosphate glasses, J. Phys. Condens. Matter 9 (1997) 6711–6718 http://stacks.iop.org/0953-8984/9/i=31/a=021.

[59] C.R. Kesavulu, R.P.S. Chakradhar, C.K. Jayasankar, J.L. Rao, EPR, optical, photolumines-cence studies of Cr^{3+} ions in Li_2O-Cs_2O-B_2O_3 glasses—an evidence of mixed alkali effect, J. Mol. Struct. 975 (2010) 93–99, https://doi.org/10.1016/j.molstruc.2010.03.091.

[60] C. Legein, J. Buzare, J. Emery, C. Jacoboni, Electron paramagnetic resonance determination of the local field distribution acting on Cr^{3+} and Fe^{3+} in transition metal fluoride glasses (TMFG), J. Phys. Condens. Matter 7 (1995) 3853–3862, https://doi.org/10.1088/0953-8984/7/20/006.

[61] C.R. Kesavulu, R.P.S. Chakradhar, R.S. Muralidhara, J.L. Rao, R.V. Anavekar, EPR, optical absorption and photoluminescence properties of Cr^{3+} ions in lithium borophosphate glasses, J. Alloys Compd. 496 (2010) 75–80, https://doi.org/10.1016/j.jallcom.2010.02.119.

[62] M.V. Sambasiva Rao, C. Rajyasree, T. Narendrudu, S. Suresh, A. Suneel Kumar, N. Veera-iah, et al., Physical and spectroscopic properties of multi-component Na_2O-PbO-Bi_2O_3-SiO_2 glass ceramics with Cr_2O_3 as nucleating agent, Opt. Mater. 47 (2015) 315–322, https://doi.org/10.1016/j.optmat.2015.05.048.

[63] S. Morimoto, S. Khonthon, Y. Ohishi, Optical properties of Cr^{3+} ion in lithium metasilicate $Li_2O \cdot SiO_2$ transparent glass-ceramics, J. Non-Cryst. Solids 354 (2008) 3343–3347, https://doi.org/10.1016/j.jnoncrysol.2008.01.025.

[64] V. Castaing, A.D. Sontakke, A.J. Fernández-Carrión, N. Touati, L. Binet, M. Allix, et al., Persistent luminescence of $ZnGa_2O_4$:Cr^{3+} transparent glass ceramics: effects of excitation wavelength and excitation power, Eur. J. Inorg. Chem. 2017 (2017) 5114–5120, https://doi.org/10.1002/ejic.201700841.

[65] D. Gourier, A. Bessière, S.K. Sharma, L. Binet, B. Viana, N. Basavaraju, et al., Origin of the visible light induced persistent luminescence of Cr^{3+}-doped zinc gallate, J. Phys. Chem. Solid 75 (2014) 826–837, https://doi.org/10.1016/j.jpcs.2014.03.005.

[66] H.A. Buckmaster, Y.H. Shing, A survey of the EPR spectra of Gd^{3+} in single crystals, Phys. Status Solidi 12 (1972) 325–361, https://doi.org/10.1002/pssa.2210120202.

[67] D. Furniss, E.A. Harris, D.B. Hollis, EPR of Gd^{3+} and Eu^{2+} in fluorozirconate glasses, J. Phys. C Solid State Phys. 20 (1987) L147–L150, https://doi.org/10.1088/0022-3719/20/10/002.

[68] C. Legein, J.Y. Buzaré, G. Silly, C. Jacoboni, The local field distribution of Gd^{3+} in tran-sition metal fluoride glasses investigated by electron paramagnetic resonance, J. Phys. Con-dens. Matter 8 (1996) 4339–4350, https://doi.org/10.1088/0953-8984/8/23/023.

[69] C.M. Brodbeck, L.E. Iton, The EPR spectra of Gd^{3+} and Eu^{2+} in glassy systems, J. Chem. Phys. 83 (1985) 4285, https://doi.org/10.1063/1.449041.

[70] H. Ebendorff-Heidepriem, D. Ehrt, Electron spin resonance spectra of Eu^{2+} and Tb^{4+} ions in glasses, J. Phys. Condens. Matter 11 (1999) 7627, https://doi.org/10.1088/0953-8984/11/39/317.

[71] S. Simon, A.D. Udvar, Effect of gadolinium on the structure and magnetic properties of glass and glass-ceramic sillenites, J. Am. Ceram. Soc. 93 (2010) 2760–2763, https://doi.org/10.1111/j.1551-2916.2010.03783.x.

[72] A. Fedotovs, A. Antuzevics, U. Rogulis, M. Kemere, R. Ignatans, Electron paramagnetic resonance and magnetic circular dichroism of Gd^{3+} ions in oxyfluoride glass-ceramics con-

taining CaF_2 nanocrystals, J. Non-Cryst. Solids 429 (2015) 118–121, https://doi.org/10.1016/j.jnoncrysol.2015.08.036.

[73] A. Antuzevics, M. Kemere, R. Ignatans, Local structure of gadolinium in oxyfluoride glass matrices containing SrF_2 and BaF_2 crystallites, J. Non-Cryst. Solids 449 (2016) 29–33, https://doi.org/10.1016/j.jnoncrysol.2016.07.015.

[74] S.A. Al'tshulter, B.M. Kozyrev, Electron Paramagnetic Resonance in Compounds of Transition Elements, Wiley, 1974.

[75] R.D. Shannon, Revised effective ionic radii and systematic studies of interatomic distances in halides and chalcogenides, Acta Crystallogr. A 32 (1976) 751–767, https://doi.org/10.1107/S0567739476001551.

[76] C. Yang, S. Lee, A.J. Bevolo, Investigations of the weak trigonal Gd^{3+} ESR center in alkaline-earth fluoride crystals, Phys. Rev. B 13 (1976) 2762–2767.

[77] P. Pascuta, E. Culea, Effect of gadolinium ions on the structure and magnetic properties of zinc-borate glasses and glass ceramics, J. Mater. Sci. 47 (2012) 2345–2351, https://doi.org/10.1007/s10853-011-6051-1.

[78] M. Bosca, L. Pop, L. Bolundut, N. Tothazan, G. Borodi, I. Vida-Simiti, et al., Effects of Gd^{3+}: Ag co-doping on structural and magnetic properties of lead tellurite glass ceramics, Ceram. Int. 42 (2016) 1169–1176, https://doi.org/10.1016/j.ceramint.2015.09.047.

[79] S. Schweizer, G. Corradi, A. Edgar, J.-M. Spaeth, EPR of Eu^{2+} in $BaBr_2$ crystals and fluorobromozirconate glass ceramics, J. Phys. Condens. Matter 13 (2001) 2331–2338, https://doi.org/10.1088/0953-8984/13/10/323.

[80] Z. Lin, H. Zeng, Y. Yang, X. Liang, G. Chen, L. Sun, The effect of fluorine anions on the luminescent properties of Eu-doped oxyfluoride aluminosilicate glasses, J. Am. Ceram. Soc. 93 (2010) 3095–3098, https://doi.org/10.1111/j.1551-2916.2010.04067.x.

[81] C. Zhu, D. Wu, Y. Zhang, M. Zhang, Y. Yue, Composition dependence of the optical and structural properties of Eu-doped oxyfluoride glasses, J. Alloys Compd. 632 (2015) 291–295, https://doi.org/10.1016/j.jallcom.2015.01.207.

[82] Q. Luo, X. Qiao, X. Fan, S. Liu, H. Yang, X. Zhang, Reduction and luminescence of europium ions in glass containing SrF_2 nanocrystals, J. Non-Cryst. Solids 354 (2008) 4691–4694, https://doi.org/10.1016/j.jnoncrysol.2008.07.019.

[83] Q. Luo, X. Qiao, X. Fan, X. Zhang, Luminescence properties of Eu^{2+}-doped glass ceramics containing SrF_2 nanocrystals, J. Am. Ceram. Soc. 93 (2010) 2684–2688, https://doi.org/10.1111/j.1551-2916.2010.03756.x.

[84] K. Biswas, A.D. Sontakke, R. Sen, K. Annapurna, Luminescence properties of dual valence Eu doped nano-crystalline BaF_2 embedded glass-ceramics and observation of $Eu^{2+} \rightarrow Eu^{3+}$ energy transfer, J. Fluoresc. 22 (2012) 745–752, https://doi.org/10.1007/s10895-011-1010-4.

[85] A. Antuzevics, M. Kemere, G. Krieke, R. Ignatans, Electron paramagnetic resonance and photoluminescence investigation of europium local structure in oxyfluoride glass ceramics containing SrF_2 nanocrystals, Opt. Mater. 72 (2017) 749–755, https://doi.org/10.1016/j.optmat.2017.07.024.

[86] V. Pukhkaya, , Influence of Yb^{3+} and Er^{3+} Ions Environment on the Evolution of Its' Luminescent Properties in Oxide Glasses Under Ionizing Irradiation, Doctoral dissertation, Ecole Polytechnique X, 2013.

[87] C. Lin, L. Calvez, Z. Li, S. Dai, H. Tao, H. Ma, et al., Enhanced up-conversion luminescence in Er^{3+}-doped $25GeS_2 \cdot 35Ga_2S_3 \cdot 40CsCl$ chalcogenide glass-ceramics, J. Am. Ceram. Soc. 96 (2013) 816–819, https://doi.org/10.1111/jace.12102.

[88] G. Dantelle, M. Mortier, D. Vivien, EPR and optical studies of erbium-doped β-PbF$_2$ single-crystals and nanocrystals in transparent glass–ceramics, Phys. Chem. Chem. Phys. 9 (2007) 5591, https://doi.org/10.1039/b706735f.

[89] U. Rogulis, A. Fedotovs, A. Antuzevics, D. Berzins, Y. Zhydachevskyy, Optical detection of paramagnetic centres in activated oxyfluoride glass-ceramics, Acta Phys. Pol. A 133 (2018) 785–788, https://doi.org/10.12693/APhysPolA.133.785.

[90] U. Rogulis, Optical detection of paramagnetic centres: from crystals to glass-ceramics, Fiz. Nizk. Temp. 42 (2016) 689–693, https://doi.org/10.1063/1.4959009.

[91] U. Ranon, W. Low, Electron spin resonance of Er^{3+} in CaF$_2$, Phys. Rev. 132 (1963) 1609–1611, https://doi.org/10.1103/PhysRev.127.1892.

[92] V. Pukhkaya, P. Goldner, A. Ferrier, N. Ollier, Impact of rare earth element clusters on the excited state lifetime evolution under irradiation in oxide glasses, Opt. Express 23 (2015) 3270, https://doi.org/10.1364/OE.23.003270.

[93] N. Ollier, J.L. Doualan, V. Pukhkaya, T. Charpentier, R. Moncorgé, S. Sen, Evolution of Yb^{3+} environment and luminescence properties under ionizing irradiation in aluminoborosilicate glasses, J. Non-Cryst. Solids 357 (2011) 1037–1043, https://doi.org/10.1016/j.jnoncrysol.2010.11.041.

[94] G. Dantelle, M. Mortier, P. Goldner, D. Vivien, EPR and optical study of Yb^{3+}-doped β-PbF$_2$ single crystals and nanocrystals of glass-ceramics, J. Phys. Condens. Matter 18 (2006) 7905–7922, https://doi.org/10.1088/0953-8984/18/34/005.

[95] M. Karabulut, A. Popa, G. Borodi, R. Stefan, An FTIR and ESR study of iron doped calcium borophosphate glass-ceramics, J. Mol. Struct. 1101 (2015) 170–175, https://doi.org/10.1016/j.molstruc.2015.08.004.

[96] S. Khonthon, S. Morimoto, Y. Arai, Y. Ohishi, Luminescence characteristics of Te- and Bi-doped glasses and glass-ceramics, J. Ceram. Soc. Jpn. 115 (2007) 259–263, https://doi.org/10.2109/jcersj.115.259.

[97] A. Suneel Kumar, T. Narendrudu, S. Suresh, M.V. Sambasiva Rao, G. Chinna Ram, D. Krishna Rao, Role of titanium ions on the physical and structural properties of calcium zinc bismuth phosphate glass ceramics, J. Non-Cryst. Solids 434 (2016) 62–70, https://doi.org/10.1016/j.jnoncrysol.2015.12.010.

[98] M. Nikl *Nanocomposite, Ceramic, and Thin Film Scintillators,* Pan Stanford, 2016..

[99] A. Fedotovs, U. Rogulis, A. Sarakovskis, L. Dimitrocenko, EPR of radiation defects in lithium-oxyfluoride glass ceramics, J. Phys. Conf. Ser. 249 (2010) 2–6, https://doi.org/10.1088/1742-6596/249/1/012019.

Abstract

The development of novel materials requires a profound understanding of the relationship between a material's performance and its structural properties. Electron paramagnetic resonance (EPR) is a well-established technique for a direct detection and identification of paramagnetic defects in solids. This chapter provides an overview of the applicability of continuous wave EPR spectroscopy in the studies of glass ceramics focusing on transition metal (Mn^{2+}, Cu^{2+}, Cr^{3+}) and rare earth (Gd^{3+}, Eu^{2+}, Er^{3+}, Yb^{3+}) ion local structure analysis. EPR spectra features of the above-mentioned paramagnetic probes in glasses and glass ceramics are compared and discussed in detail. The chapter also serves the purpose of summarizing recent endeavors devoted to the investigation of transparent glass ceramics illustrating the results on oxyfluoride glass ceramic systems.

Keywords: Electron paramagnetic resonance; Electron spin resonance; Electron magnetic resonance; Transparent glass ceramics; Paramagnetic centers; Defect local structure